

## A Boundary-Layer Model for Mars: Comparison with Viking Lander and Entry Data

ROBERT M. HABERLE

*Space Sciences Division, NASA/Ames Research Center, Moffett Field, California*

HOWARD C. HOUBEN

*Space Physics Research Institute, Sunnyvale, California*

ROLF HERTENSTEIN

*Department of Meteorology, San Jose State University, San Jose, California*

TOMAS HERDTLE\*

*Department of Physics, University of California at Berkeley, Berkeley, California*

(Manuscript received 7 October 1991, in final form 10 August 1992)

### ABSTRACT

A one-dimensional boundary-layer model for Mars is described, and its results are compared with Viking data. The model equations are similar to Earth boundary-layer models in that they include contributions from Coriolis, pressure gradient, and frictional forces for momentum; and radiation, sensible heat flux convergence, and advection for heat. Turbulent fluxes are computed from the level-2 second-order closure theory of Mellor and Yamada with similarity relations employed for boundary conditions. The pressure gradient force can be specified or computed from a simple slope model. Radiative heating is due to the absorption of solar and infrared radiation by CO<sub>2</sub> gas and suspended dust particles. Ground temperatures are computed by solving a surface heat budget using an accurate treatment of conduction into the Martian soil.

The data used for comparison were obtained by the Viking 1 and 2 landers for early northern summer. At each site, these data include a single profile of wind and temperature between 1.5 and 4 km and their diurnal variations at 1.6 m above the surface. Model-predicted temperatures are in good agreement with the data, though they show a greater variation at 1.6 m than is evident in the data. Model-predicted winds compare less favorably in that they can match the surface data or the profiles, but not both simultaneously. In addition, best agreement is obtained using a slope magnitude and/or direction that is different from reported values. However, the model can reproduce the shape, phase, and sense of rotation of the surface wind hodograph at each site. Some features of the simulations include low-level nocturnal jets, which may be common on Mars, and a negative feedback between dust and surface stress. The sensitivity of the model to uncertain parameters such as dust load, optical properties, and surface roughness is discussed.

### 1. Introduction

This paper describes a model of the Martian boundary layer and how it compares with Viking Lander observations. The purpose of the model is to provide a tool for science investigations of atmosphere-surface interactions on Mars, as well as engineering data for design studies of future Mars missions. The model incorporates the same physics as many Earth-atmosphere boundary-layer models, but with appropriate modifications for radiation and surface properties.

Previous models have focused on buoyancy-driven

boundary layers (Gierasch and Goody 1968; Flasar and Goody 1976), slope effects (Blumsack et al. 1973; Magalhaes and Gierasch 1982; Ye et al. 1990), and the influence of dust heating on surface layer properties (Pallman 1983). Here, a model is developed that combines elements of each of these studies for general applicability.

The model is one-dimensional and includes a momentum equation so that winds and surface stresses can be predicted self-consistently. The momentum equation accounts for the three dominant forces that act on winds within the boundary layer: friction, pressure gradient, and Coriolis forces. Frictional forces are computed from the level-2 turbulence closure theory of Mellor and Yamada (1974). Thus, momentum fluxes are diffusive, and the exchange coefficients are calculated from simple algebraic expressions involving the local Richardson number. The pressure-gradient

---

\* Current affiliation: Kit Corporation, 1355 Mendota Heights Road, St. Paul, MN 55120.

---

Corresponding author address: Dr. Robert M. Haberle, Ames Research Center/SST:245-3, NASA, Moffett Field, CA 94035-1000.

force can be specified (constant or time varying) or computed from a slope model.

In this paper, we calculate it from a slope model since the observations used for comparison have been interpreted in terms of a topographically controlled wind system (Hess et al. 1977; Murphy et al. 1990a). Such wind systems are likely to be much in evidence on Mars, where a large fraction of the planet's surface is sloping with typical values near 0.005. Above sloping terrain there is a component of gravity that is parallel to the ground and accelerations can arise in association with buoyancy forces due to the diurnal heating and cooling along the slope. This heating and cooling can be quite substantial on Mars because of the low thermal inertia of its surface and the low mass ( $\sim 7$  mb) and radiatively active nature of its primarily  $\text{CO}_2$  atmosphere. Its boundary layer can therefore grow to be quite deep ( $\sim 10$  km), and the resulting winds can be quite strong (tens of meters per second).

In addition to convective heating, which is also modeled using the Mellor and Yamada theory, the model includes the radiative effects of  $\text{CO}_2$  gas and suspended dust particles—the main radiatively active constituents of the Martian atmosphere. Radiative heating is significant in the Mars atmosphere because of the short associated damping times (e.g., Goody and Belton 1967). Both radiation and convection depend on surface temperatures that are computed in the model from a surface heat budget.

## 2. Model description

The Mars Planetary Boundary Layer Model is a one-dimensional (vertical) atmosphere–surface model. It numerically solves energy and momentum equations for the atmosphere and a heat conduction equation at the surface. The main output is the prediction of wind and temperature profiles in the atmosphere throughout the course of a day. These predictions can be made for any given latitude, season, and atmospheric dust loading.

The governing atmospheric momentum equations represent a balance between the three dominant forces that act on the wind field within the boundary layer: Coriolis, pressure gradient, and frictional forces. The energy equation accounts for the two principal means of energy transfer within the boundary layer: radiation and convection. The full set of equations is

$$\frac{du}{dt} = fv - fV_g + \frac{\partial}{\partial z} \left( K_M \frac{\partial u}{\partial z} \right) \quad (1)$$

$$\frac{dv}{dt} = -fu + fU_g + \frac{\partial}{\partial z} \left( K_M \frac{\partial v}{\partial z} \right) + F_y \quad (2)$$

$$\frac{d\theta}{dt} = \left( \frac{p_0}{p} \right)^{R/c_p} \dot{q} + \frac{\partial}{\partial z} \left( K_H \frac{\partial \theta}{\partial z} \right), \quad (3)$$

where  $u$  and  $v$  are the components of the horizontal

wind,  $U_g$  and  $V_g$  are the corresponding components of the geostrophic wind in balance with the large-scale pressure gradient,  $f$  is the Coriolis parameter,  $\theta$  is the potential temperature,  $\dot{q}$  is the radiative heating rate,  $p$  is the pressure,  $p_0$  is the pressure at a reference level,  $R$  is the gas constant, and  $c_p$  is the specific heat. The independent variables are time  $t$  and height  $z$ . The turbulent diffusivities of momentum  $K_M$  and heat  $K_H$  are derived from the second-order closure theory of Mellor and Yamada (1974), as described below. We also describe our derivation of the upslope forcing function  $F_y$  (the coordinate system being oriented with the  $y$  axis pointed in the uphill direction), radiation scheme, the surface heat balance model, numerical methods, and input parameters. A passive atmospheric tracer (like water vapor) could easily be included in the model. All such scalar quantities would be expected to behave in the same manner as the potential temperature [Eq. (3)].

### a. Turbulence scheme

The turbulent diffusivities of Eqs. (1)–(3) are computed from the level-2 second-order closure theory of Mellor and Yamada (1974; 1982) as functions of the gradient Richardson number:

$$\text{Ri} = \frac{\beta g \partial \theta / \partial z}{(\partial u / \partial z)^2 + (\partial v / \partial z)^2}, \quad (4)$$

where  $\beta$  is the volume expansion coefficient and  $g$  is the gravitational acceleration. The diffusivities are given by

$$K_M = l^2 \left[ \left( \frac{\partial u}{\partial z} \right)^2 + \left( \frac{\partial v}{\partial z} \right)^2 \right]^{1/2} G_M^{-1/2} S_M = ql S_M \quad (5)$$

$$K_H = l^2 \left[ \left( \frac{\partial u}{\partial z} \right)^2 + \left( \frac{\partial v}{\partial z} \right)^2 \right]^{1/2} G_M^{-1/2} S_H = ql S_H, \quad (6)$$

where the quantities  $S_M$ ,  $S_H$ , and  $G_M^{-1/2}$  are algebraic functions of the gradient Richardson number (Fig. 1),  $q^2$  is twice the turbulent kinetic energy per unit mass, and the turbulent mixing length  $l$  must be derived from still another set of relations. We have adopted the widely used, but ad hoc, prescription (Blackadar 1962)

$$l = l_0 \frac{kz}{kz + l_0}, \quad (7)$$

where  $k$  is von Kármán's constant and  $l_0$  is the maximum value the mixing length can achieve within the boundary layer. Note that the mixing length is proportional to height near the surface and approaches  $l_0$  at large values of  $z$ . The maximum mixing length is given by another widely used prescription:

$$l_0 = 0.2 \frac{\int_0^\infty qz dz}{\int_0^\infty q dz}. \quad (8)$$

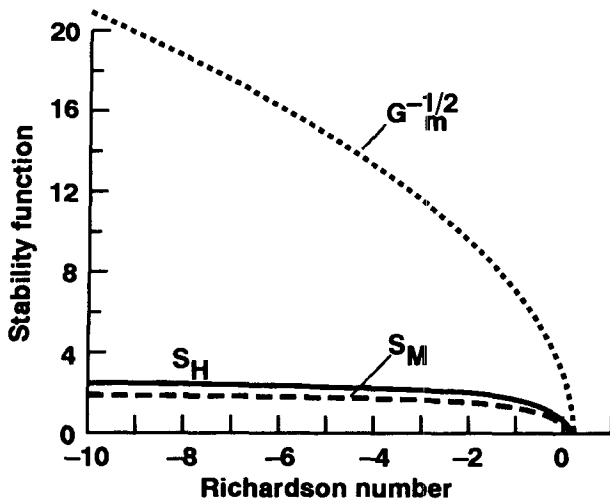


FIG. 1. Stability functions from the level-2 turbulence closure theory of Mellor and Yamada (1974).

In the level-2 formalism, turbulent kinetic energy is calculated assuming a balance between production and dissipation. Above a critical value for the gradient Richardson number ( $Ri_c$ ), all turbulence is extinguished. In the present application  $Ri_c = 0.19$  (Mellor and Yamada 1982).

To complete the scheme the turbulent fluxes must be prescribed at the top and bottom boundaries of the model. We require these fluxes to vanish at the top of the model (which is at 40 km, well above the maximum boundary-layer height). At the surface, the fluxes are given by drag laws derived from Monin-Obukhov similarity theory (e.g., Arya 1988):

$$K_M \left( \frac{\partial u}{\partial z}, \frac{\partial v}{\partial z} \right) = u_*^2 (\cos \eta, \sin \eta) \quad (9)$$

and

$$K_H \left( \frac{\partial \theta}{\partial z} \right) = u_* \theta_*, \quad (10)$$

where

$$u_* = c_d \sqrt{u_s^2 + v_s^2} \quad (11)$$

and

$$\theta_* = c_h (T_s - T_g). \quad (12)$$

In the above relations, the subscript  $g$  refers to the ground, and the subscript  $s$  refers to the "screen height";  $\eta$  is the angle between the surface wind and the positive  $x$  axis. The drag coefficients  $c_d$  and  $c_h$  are functions of stability and surface roughness  $z_0$ . For the heat equation, the effect of a molecular conducting sublayer, which may be important for Mars (Sutton et al. 1978), has been included. Note that while our definition of  $c_d$

differs from convention, it is consistent with that used by Sutton et al. (1978).

### b. Upslope forcing

The effects of sloping terrain are most easily derived in a coordinate system that follows the terrain at low altitudes (Mahrer and Pielke 1977; McNider and Pielke 1981). We choose the transformed vertical coordinate

$$z^* = \lambda (e^{z/\lambda} - e^{z_g/\lambda}), \quad (13)$$

where  $z_g$  is the height of the sloping surface and the length  $\lambda$ , a measure of the depth of the surface influence, is a free parameter to be determined by comparison of model results with observations. (Any one-dimensional model of the slope effect must include a free parameter since the slope effect is fundamentally a two-dimensional phenomenon.) We orient the coordinate system with the  $y$  axis in the uphill direction and assume that (in the transformed coordinate system)  $\partial u / \partial y = \partial v / \partial y = \partial T / \partial y = 0$ . Thus, isotherms, for example, parallel the surface at low altitudes and gradually flatten out as one moves upward into the atmosphere, with an  $e$ -folding depth of  $\lambda$ . With these assumptions, we can specify the upslope forcing function:

$$F_y = -\frac{1}{\rho} \frac{\partial p}{\partial y} - g \frac{\partial z}{\partial y}, \quad (14)$$

while the remainder of Eqs. (1)–(3) are unchanged to first order in the slope  $\alpha \equiv \partial z / \partial y$ .

An integral expression for  $F_y$  can be found by use of the hydrostatic relation  $\partial p / \partial z = -\rho g$ . In the terrain-following coordinate system this leads directly to

$$\frac{\partial p}{\partial y} = \int_z^\infty \left( g \frac{\partial \rho}{\partial y} - \frac{\alpha}{\lambda} e^{-z/\lambda} \rho g \right) dz. \quad (15)$$

After some manipulation of this relation, including an integration by parts, we obtain

$$F_y = \frac{1}{\rho} \int_z^\infty \frac{\rho g}{RT} \left( F_y - \alpha e^{-z/\lambda} \frac{\partial T}{\partial z} \right) dz. \quad (16)$$

For most choices of  $\lambda$ , our model top at 40 km is many  $e$ -folding depths above the surface. In this case,  $F_y$  is small at the upper boundary, and we can calculate the integral in Eq. (16) without any problem. The coordinate system chosen by Blumsack et al. (1973) in their work on slope-induced Martian winds, on the other hand, is equivalent to the choice of  $\lambda = \infty$ . They were thus required to impose an additional condition on their model (that of zero mass convergence) in order to calculate their version of Eq. (16). This sometimes resulted in very strong upslope accelerations at high altitudes. The free parameter can clearly be avoided altogether in a two-dimensional model where the hydrostatic relation is integrated separately in different columns of the atmosphere and gradients are calculated directly.

### c. Radiation

Radiative heating in the model is due to the absorption of solar and infrared radiation by CO<sub>2</sub> gas and suspended dust particles. Both constituents are assumed to be uniformly distributed in height. The code used to calculate these heating rates is taken from Haberle and Jakosky (1991) to which the reader is referred for details. Here, a brief discussion of the basic model is presented.

At solar wavelengths we first compute the amount of absorption due to CO<sub>2</sub> alone and then use the remaining flux to calculate the absorption due to dust. This simplifies the calculations and is justified to first order since most of the gaseous absorption takes place at high levels (>20 km) and is small in comparison to dust absorption. Carbon dioxide absorption is based on the equivalent widths of the near infrared bands as described in Pollack et al. (1981). Dust absorption is calculated from a "lookup" table, created off-line with a doubling code using the single-scattering properties and phase functions determined from Viking Lander imaging data (Pollack et al. 1979).

In the infrared, two broad spectral intervals are considered: the 15- $\mu$ m band of CO<sub>2</sub> (477–857 cm<sup>-1</sup>), and everything else. Dust and CO<sub>2</sub> are optically active within the 15- $\mu$ m band, while only dust is active outside it. Net fluxes within each of these spectral intervals are calculated by solving the transfer equation written in terms of the Planck-weighted emissivity. The emissivities were calculated off-line. Dust emissivities were calculated using a two-stream code and mean scattering properties determined from Mie theory. The particle size distribution and wavelength dependence of the refractive index were taken from Toon et al. (1977). The emissivity of CO<sub>2</sub> was calculated from the equivalent width formulation of Pollack et al. (1981), assuming a constant temperature along the absorbing path (200 K).

### d. Surface heat balance

Ground temperatures are calculated from a thermal model similar to that developed by Kieffer et al. (1977); details can be found in Haberle and Jakosky (1991). Briefly, we solve a thermal diffusion equation in the soil at 12 different levels down to a depth of 10 times the diurnal skin depth ( $\sim 5$  cm for typical Martian soil). Soil properties are assumed to be homogeneous. The boundary condition at the surface balances the upward flux of conducted energy with the net radiative and convective losses. At depth, the conducted energy vanishes.

### e. Numerical methods

To apply the above equations, the atmosphere is divided into 85 layers extending from the surface to 40 km. This height is well above the deepest boundary

layer anticipated ( $\sim 15$  km), yet well below the level for which non-LTE radiative transfer must be considered ( $\sim 80$  km). The thickness of each layer increases with height such that greatest vertical resolution occurs near the surface. The lowest model layer is chosen to be 3.2-m thick, so that the variables predicted for this layer can be directly compared with Viking Lander meteorological data taken 1.6 m above the surface.

Equations (1)–(3) are each examples of a diffusion equation. We have therefore chosen to solve a single generalized diffusion equation with sources and sinks whose coefficients depend on the variable being solved. The code has been written in this manner to facilitate the incorporation of additional variables, such as dust and water. The generalized diffusion equation is solved using forward time differences and centered space differences but with a Crank–Nicholson-type weighting function for variables not involved in the time derivatives. In its current configuration, 1-minute time steps and a Crank–Nicholson weighting factor appropriate for fully implicit schemes are used.

### f. Model parameters

Nominal model input parameters are given in Table 1. These values are appropriate to the Viking Lander sites during early northern summer. The surface pressure and visible dust optical depth were taken directly from Viking measurements (Colburn et al. 1989) and represent the approximate daily average value for the given seasonal date. Model results are sensitive to the dust optical depth, which varied by as much as several tenths during this period. Pressure fluctuations were relatively small (<0.1 mb), however, and have little effect on model results. Values for the surface albedo, thermal inertia, and ratio of visible to infrared dust opacity were chosen to reproduce observed surface temperatures (e.g., Haberle and Jakosky 1991). This was done to provide a means of imposing the correct boundary forcing and is not, therefore, a test of the model itself. The nominal surface roughness was taken to be 1 cm. This is the largest value used by Sutton et al. (1978) but is not necessarily an upper limit.

TABLE 1. Nominal model input parameters.

Parameter	VL-1	VL-2
Latitude	23°N	48°N
Season	$L_S = 110^\circ$	$L_S = 130^\circ$
Surface pressure (Pa)	730	800
Visible dust opacity	0.4	0.3
Surface albedo	0.32	0.34
Thermal inertia (SI)	215	240
Vis/IR dust opacity	2.0	2.0
Surface roughness (m)	0.01	0.01
Slope	0.003 down to NE	0.002 down to SW
Geostrophic wind	0.0	0.0
Isotherm $e$ -fold depth (km)	7	7

In all results, the winds are driven by the physics of the slope model. The main inputs are magnitude and direction of the sloping terrain and the value of  $\lambda$ , the isotherm  $e$ -folding depth. For the *Viking Lander-1* site best results are obtained with  $\lambda = 7$  km and terrain that slopes downward toward the northeast with a magnitude 0.003. Hess et al. (1977) report the same downslope direction for this site, but with a much steeper gradient (0.015). However, use of this gradient in our model produces unrealistically strong surface winds (see Fig. 9), and trade-offs between slope magnitude and  $\lambda$  do not improve the agreement. At the *Viking Lander-2* site we obtain good results using the reported slope magnitude and the same value of  $\lambda$  but require a different downslope direction to match the phase of the observed diurnal surface wind variation. The discrepancies associated with the topographic slopes are discussed in section 5.

After specifying these parameters the model is spun up from a resting isothermal (200 K) initial state for a period of 6 days. By the sixth day the diurnal cycle very closely repeats itself; temperatures within the boundary layer are repeatable to within  $\sim 0.2$  K, and winds to within  $\sim 0.5$  m s $^{-1}$ . All results are presented for the sixth day. The results are insensitive to the initial temperature as long as it is chosen to be close the daily- and vertically averaged value.

### 3. Comparison with observations

We compare model predictions of wind and temperature with those observed by the two Viking Landers during their descent to the surface and shortly thereafter. Both landers touched down in the Northern Hemisphere during summer (Table 1). Entry times were 1615 LLT at *Viking Lander 1* (VL-1) and 0945 LLT at *Viking Lander 2* (VL-2).<sup>1</sup> Since the descent to the surface took less than several minutes, the entry measurements are considered simultaneous. However, the surface measurements did not begin immediately after touchdown because of the time required to deploy the boom-mounted meteorology package. We have assumed that the surface measurements obtained on the following day at the same time are representative of those on the day of entry. The entry data are described by Seiff and Kirk (1977) and Seiff (1993), whereas the surface data can be found in Hess et al. (1977) and Sutton et al. (1978).

#### a. VL-1

Simulated temperatures are compared with the entry data in Fig. 2. The entry data has errors on the order  $\pm 1$  K. The simulated late afternoon temperature profile

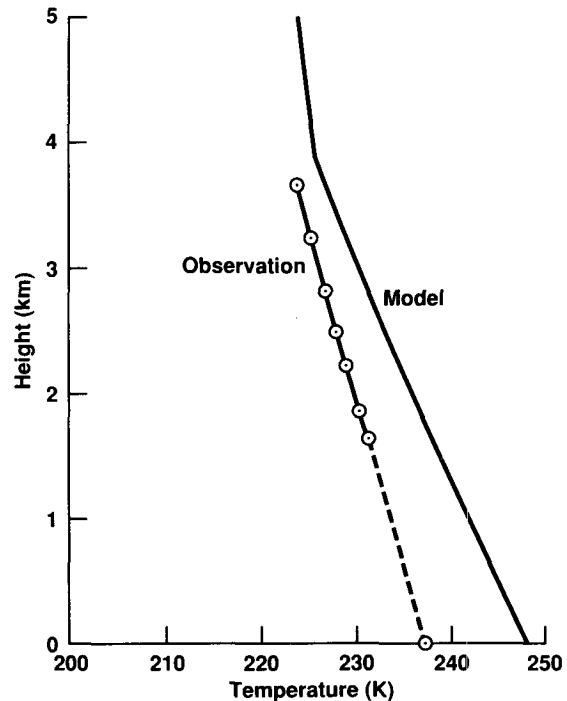


FIG. 2. Comparison of the simulated temperature profile at 1615 local time (solid) with the VL-1 entry data (solid-dashed). Open circles represent selected measurements. The dashed line represents a linear interpolation from the last value measured before the descent engines fired, to the 1.6-m temperature measured on the following day at the same local time.

is warmer and less stable than the observed profile. The model profile is slightly superadiabatic, while the observed profile is slightly subadiabatic. The model boundary layer is close to its maximum depth of 4 km at this time (Fig. 3). However, the observations suggest an even deeper boundary layer as near-neutral conditions persist up to 6.5 km (Seiff and Kirk 1977; Seiff 1993).

Simulated 1.6-m temperatures are compared with the meteorology data in Fig. 4. At VL-1 the meteorology data are accurate to  $\pm 1.5$  K. The model tends to overestimate the near-surface temperature amplitude, being warmer than the observations during the day and cooler at night. Simulated mean temperatures, however, are in good agreement. Temperature differences between the model and observations are largest at entry time.

Since we have constrained surface temperatures to match the observations, the excessive diurnal amplitudes are due to errors in the radiative heating rates, or to errors in the turbulent heat flux convergence. The former are dominated by CO $_2$  infrared heating (see Fig. 20). However, the band model used to compute this heating tends to underestimate absorption for the very short (meters) path lengths considered in this work (Crisp 1986). We therefore suspect that errors in the turbulence scheme are more important. The surface

<sup>1</sup> The length of a Martian solar day is 88 775 s. All times are based on a 24-hour Martian day. LLT stands for Local Lander Time in which noon occurs when the sun is directly overhead.

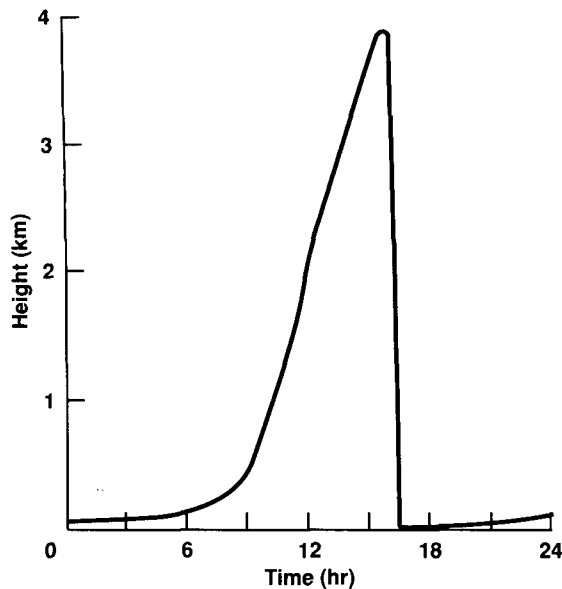


FIG. 3. Simulated diurnal variation of the boundary-layer depth at *VL-1*. The boundary-layer depth is defined as that height above the surface where the gradient Richardson number ( $Ri$ ) first exceeds the critical gradient Richardson number ( $Ri_c$ ).

sensible heat flux is shown in Fig. 5 and is consistent with that derived by Sutton et al. (1978). Thus, the level-2 turbulence scheme appears to underestimate mixing. Stronger upward daytime fluxes would bring the model more in line with observations; the static stability would be lower, the boundary layer would be deeper, and the 1.6-m temperatures would be cooler.

Simulated wind profiles are shown in Fig. 6 along with selected inferred entry velocities. The latter were recently derived by Seiff (1993) from an analysis of the radar tracking data during the parachute phase of the descent. The inferred winds have an estimated ac-

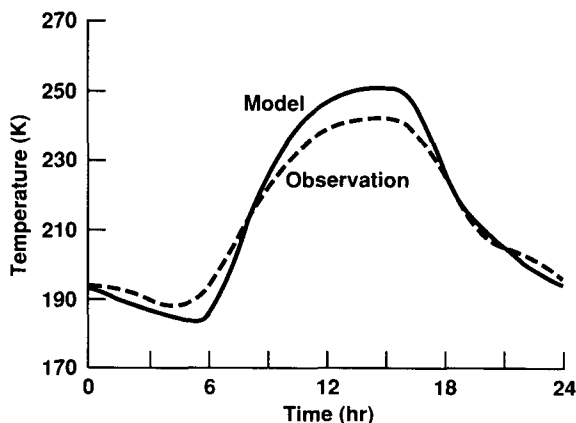


FIG. 4. Comparison of the simulated 1.6-m diurnal temperature variation (solid) with *VL-1* meteorology data (dashed). The meteorology data represent a composite of the first 15 sols. They have been grouped into 25 "hourly" time bins and then smoothed using a fifth-order least squares fit (Sutton et al. 1978).

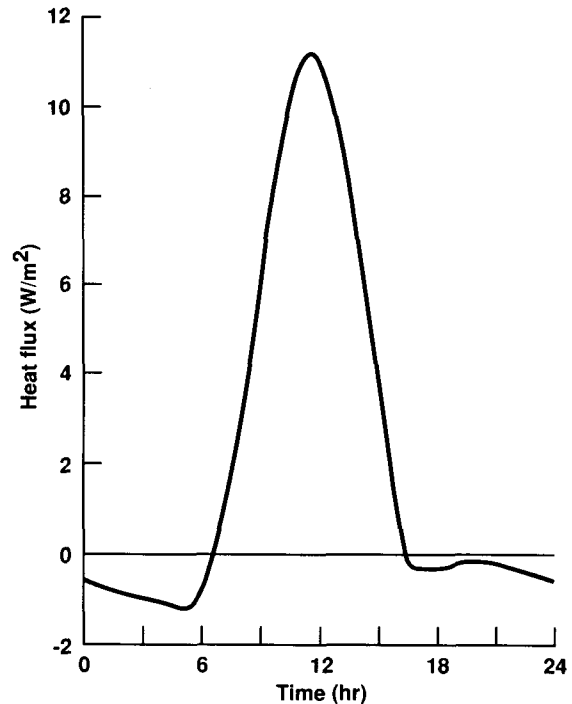


FIG. 5. Simulated diurnal variation of the surface sensible heat flux at *VL-1*.

curacy of  $\pm 3 \text{ m s}^{-1}$ . Both model and observations show southeasterly winds between 1.5 and 3 km. This is the expected direction of the steady component of a slope-driven wind system whose terrain slopes downward toward the northeast as it does at *VL-1* (see Hess et al. 1977). However, the modeled winds are much weaker than observed. Furthermore, the rotation of

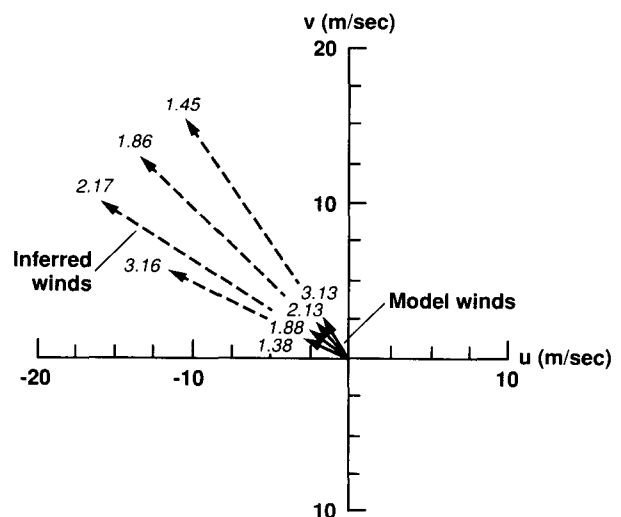


FIG. 6. Comparison of simulated winds aloft (solid) with selected inferred winds from the *VL-1* entry data (dashed). The latter are taken from Seiff (1993). Numbers at the tip of the wind vector represent altitude above the surface in kilometers.

the wind vector with height in the model is opposite the observations—clockwise rather than counterclockwise. The non-Ekman-like behavior of the observed profile could be due to cold air advection from the southeast—a process not included in the model.

At the surface model winds are in good agreement with observations (Fig. 7). The latter are accurate to  $\pm 10\%$ . The model shows a counterclockwise rotation of the surface wind vector with time that is very similar to the observed rotation. At night a downslope component develops that gradually increases after sunrise, reaching a maximum several hours before noon. The boundary layer is growing at this time (Fig. 3), so that coupling to the winds aloft begins to influence the rotation of the surface wind vector. Winds in the lowest several kilometers are southeasterly during this period and when mixed to the surface they force a counterclockwise turning of the wind.

However, at the *VL-1* entry time, the model boundary layer is still deep and active, and much of the shear in the wind field has been mixed out by turbulence (Fig. 8). This may partly explain why the model winds aloft are so much smaller than observed; momentum is mixed so efficiently during the day that very little shear can develop within the boundary layer. This may also explain why use of the slope magnitudes reported by Hess et al. (1977)—0.015—gives poor agreement with the observed surface winds. Slopes this steep produce strong winds aloft, which when mixed to the surface produce values much greater than observed (Fig. 9).

Thus, the twin constraints of relatively strong parachute velocities and weak surface winds are very difficult to satisfy in this model. It suggests that 1) mixing of momentum in the model is too strong, 2) that other processes not included in the model are important (e.g., large-scale circulation), or that 3) the single-shot nature of the inferred profiles may not be representative of

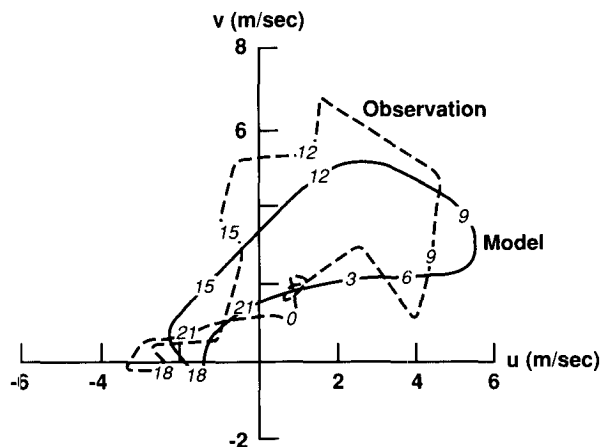


FIG. 7. Comparison of simulated (solid) and observed (dashed) wind hodographs at 1.6 m for the *VL-1* site. Local times are indicated at 3-h intervals.

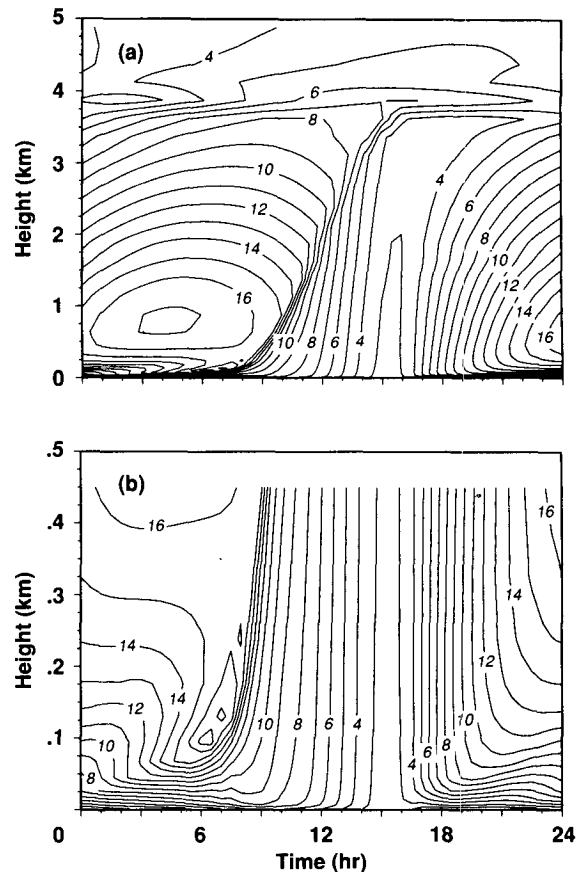


FIG. 8. Simulated time-height variation of the wind speed at *VL-1*. In (a) values are plotted to 5 km; in (b) values are plotted to 0.5 km. Contour intervals are  $1 \text{ m s}^{-1}$ .

average conditions. Without more detailed observations we cannot distinguish between these possibilities. Our approach has been to emphasize the surface data, which is much more complete.

#### b. *VL-2*

The simulated temperature profile at entry time for *VL-2* is shown in Fig. 10 and is in good agreement with observations. Simulated temperatures above 1.5

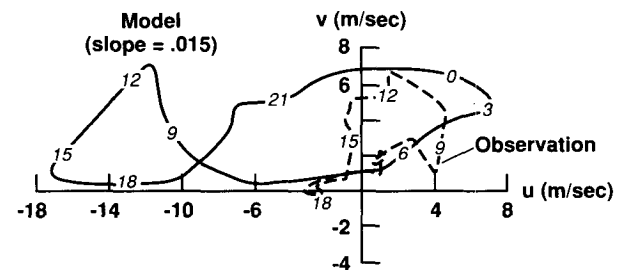


FIG. 9. Simulated 1.6-m hodograph (solid) at *VL-1* using the slope magnitude (0.015) reported by Hess et al. (1977). The observed hodograph (dashed) is shown for comparison.

km are within several degrees of the observed values, which have a similar accuracy to those at *VL-1*. There are no actual measurements below 1.5 km, where the model suggests there is an inversion at this time. Given the strong radiational cooling of the ground at night and a surface-directed sensible heat flux, formation of a low-level inversion is likely. According to the model, the depth of the inversion is about 1 km, consistent with the observations as well as other predictions (Gierasch and Goody 1968; Pollack et al. 1979; Ye et al. 1990).

The simulated *VL-2* diurnal temperature variation at 1.6 m is compared with observations in Fig. 11. Temperature errors at the *VL-2* site are  $\pm 2$  K, slightly greater than at *VL-1*. Unlike the situation for *VL-1*, the entry time at *VL-2* is very close to the time of best agreement between model and observations. However, the model still appears to overestimate the amplitude of the diurnal cycle.

The simulated surface winds for the *VL-2* site are compared with observations in Fig. 12. The observational accuracy is similar to that at *VL-1* ( $\pm 10\%$ ). The model reproduces the observed clockwise rotation of the surface wind and predicts magnitudes in approximate accord with the observations. However, daytime upslope winds are about twice the observed values. At both sites, the surface wind rotates clockwise during the night when coupling to winds aloft is expected to be minimal. However, the rate of rotation is greater at

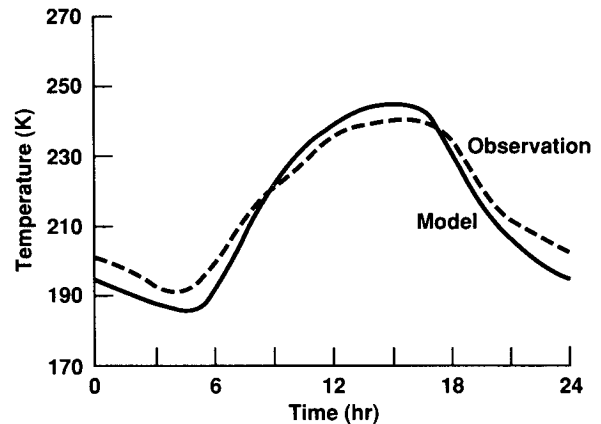


FIG. 11. As in Fig. 4 but for the *VL-2* site.

the *VL-2* site because of the Coriolis effect. The phasing is such that when coupling does occur, the surface wind must rotate clockwise at *VL-2* (counterclockwise at *VL-1*) in order to acquire the direction of the winds aloft.

As was the case for the *VL-1* simulation, we have had to use a topography for the *VL-2* simulation that is different from that reported by Hess et al. (1977). In this case, however, we require a different direction rather than a different magnitude. Use of the reported downslope direction resulted in a wind field  $90^\circ$  out of phase with the observations. At 0900 LLT, for example, surface winds were eastward instead of northward. In order to reproduce the observed direction, the model requires the downslope direction at *VL-2* to be toward the southwest rather than northwest. This gives the correct phasing of the surface wind hodograph, and

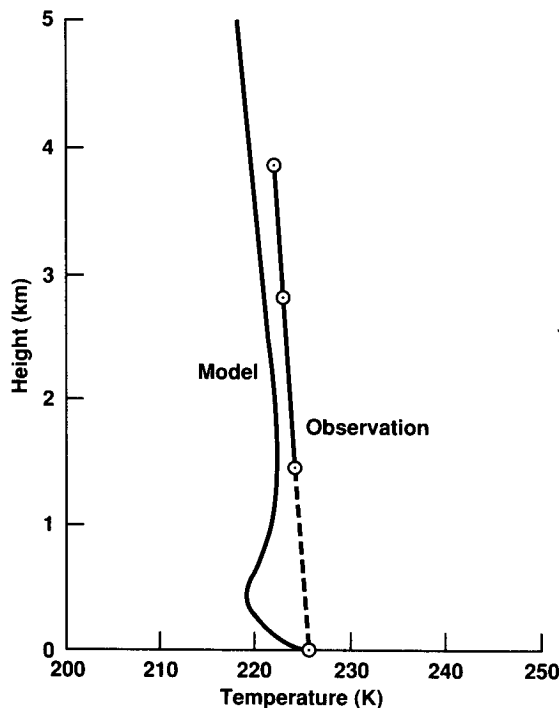


FIG. 10. As in Fig. 2 but for the *VL-2* site and a local time of 0945.

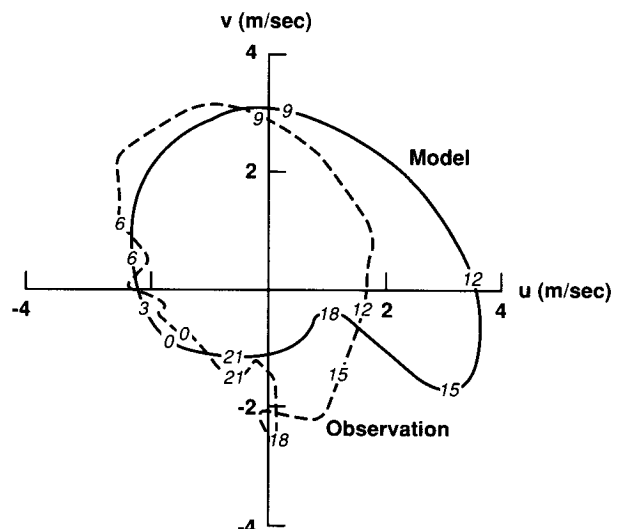


FIG. 12. As in Fig. 7 but for the *VL-2* site.



it also improves the directional agreement with the inferred winds aloft (see below). The downslope direction at the *VL-2* site is even less certain than at *VL-1* (Hess et al. 1977).

Simulated winds aloft at *VL-2* are compared with those inferred during the parachute descent in Fig. 13. The estimated accuracy of the inferred winds at this site is  $\pm 1 \text{ m s}^{-1}$ , much better than at *VL-1*. However, the comparison is similar: the model winds have the same direction as the inferred winds (only if we use a downslope direction toward the southwest), but lack their strength. The discrepancy is not as pronounced in this case but is still a factor of 2 or so. Since the boundary layer is relatively shallow at this time (Fig. 14), the low modeled wind shears cannot be due to coupling with the winds aloft. However, the boundary layer does grow through the region of measured winds at later times. Evidently forcing by the slope-induced pressure gradients is not strong enough to accelerate the winds to the observed values after the boundary layer collapses in the late afternoon. However, it is not clear whether the problem is with the slope model or the turbulence parameterization, since weaker daytime mixing would give the same effect.

#### 4. Sensitivity to selected parameters

##### a. Dust loading

By altering the deposition of solar energy and thermal emissivity of the atmosphere, dust particles can have a profound effect on atmospheric temperatures (e.g., Gierasch and Goody 1972; Pollack et al. 1979). Wind systems can also be affected (Haberle et al. 1982; Pollack et al. 1990). To estimate the model sensitivity to dust at this season, we have performed simulations for opacities of 0 and 1, holding all other input parameters as listed in Table 1. This represents the maximum range of plausible values for this season (Colburn et al. 1989).

The effect of dust on temperature profiles at the *VL-1* entry time is shown in Fig. 15. With no dust in the

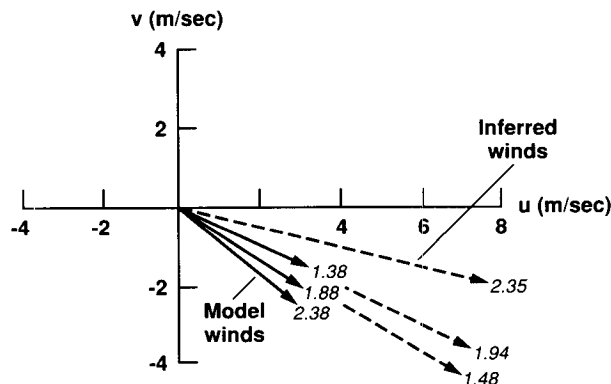


FIG. 13. As in Fig. 6 but for the *VL-2* site.

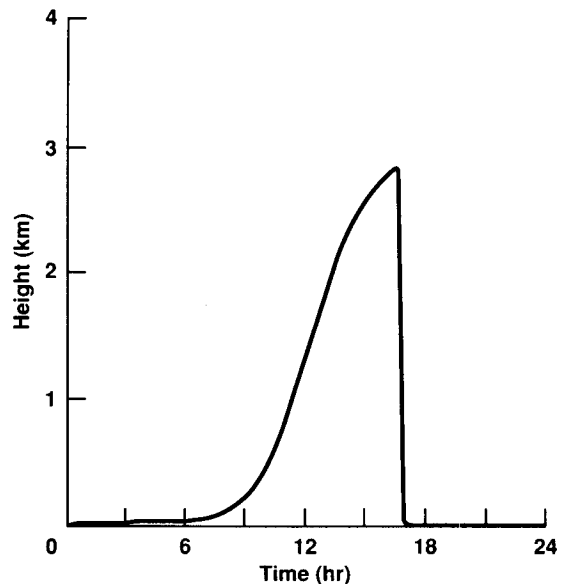


FIG. 14. As in Fig. 3 but for the *VL-2* site.

atmosphere, the vertically averaged temperature is closer to that observed, but the static stability is still too low. With moderate amounts of dust in the atmosphere (the optical depth 1 case), mean tempera-

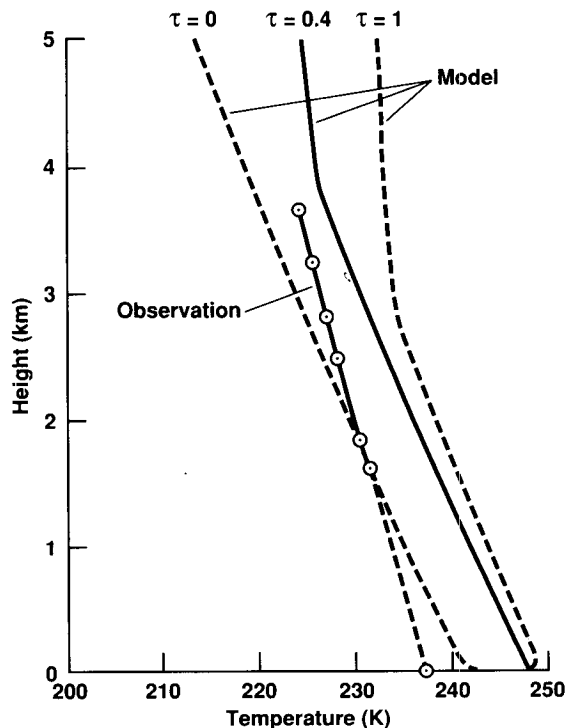


FIG. 15. Simulated *VL-1* temperature profiles at entry time for three different values of the dust optical depth: 0, 0.4, and 1.0. The solid line is from the nominal model. *VL-1* entry data (solid/dashed) are shown for comparison.

tures are about 10 K too warm. Although the static stability is still too low in the dusty experiment, the depth of the unstable region is considerably reduced. For clear conditions, the boundary layer grows to about 6 km during the day, while for optical depth 1 it only grows to about 3 km. The reduction is a consequence of an increase in the direct heating of the atmosphere and a decrease in the surface heat flux.

The slope winds are also influenced by dust loading. The altered static stability and boundary-layer depth influence the temperature variation along a true horizontal surface and, hence, the pressure gradient force that drives the slope wind system (Holton 1967; Blumsack et al. 1973). In general, the slope wind magnitude is proportional to the lapse rate. Thus, the clear simulation produces stronger winds than the dusty simulation. At entry time, the 1.5 to 4 km winds in the clear simulation are about twice as large as those in the optical depth 1 simulation (Fig. 16). Wind directions, however, are similar.

The effect of dust on the rotation of the surface wind vector is shown in Fig. 17. With increasing dust, the rotation is reduced and the mean wind becomes increasingly oriented in the downslope direction. By reducing the depth of the daytime boundary layer, dust reduces the coupling to winds aloft, and so surface winds tend to blow upslope or downslope.

#### b. Surface roughness

The surface roughness of the two lander sites is not known. Sutton et al. (1978) have estimated the surface roughness by assuming the surface is flat, homogeneous, and populated with equally sized rocks. They used Viking images to estimate the rock size and number distribution and Lettau's (1969) formula for the surface roughness. On this basis they estimate values between 0.1 and 1 cm at each site. However, these are lower limits since they do not include contributions from rocks greater than 25–50 cm in size. An upper limit can be obtained by assuming the friction velocity is  $\sim 0.4$  of the mean wind rms variance (Monin and Yaglom 1971). Then for neutral conditions, the well-known logarithmic law for the surface layer wind profile can be inverted for  $z_0$  given observed mean winds at a known height (1.6 m). This method yields results between 1 and 10 cm at *VL-1* (A. R. Dobrovolskis, personal communication). Therefore, we have performed experiments for a surface roughness of 0.1 cm (smooth case) and 10 cm (rough case). These values are an order of magnitude above and below our nominal value and should represent the range of possible values.

Changes in surface roughness affect winds more than temperatures. This is mainly due to the inclusion of a molecular conducting sublayer in the surface heat flux calculations. With such a layer heat fluxes are less sensitive to the surface roughness than they are without one (Sutton et al. 1978). In the rough case, the larger

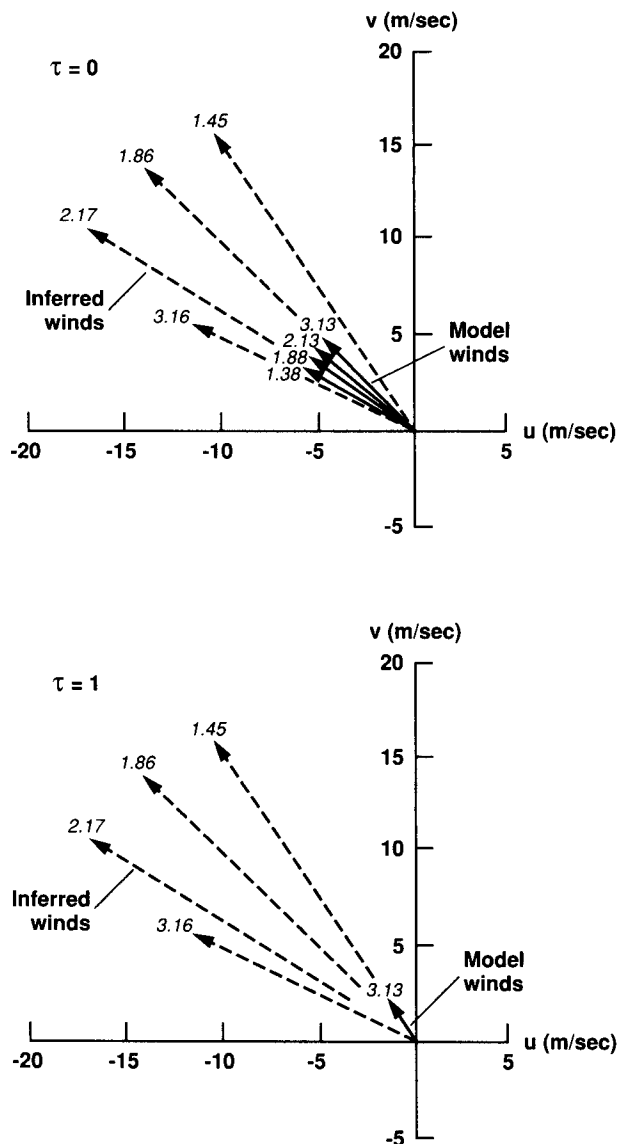


FIG. 16. Simulated *VL-1* winds (solid) in the 1.5–4-km region at entry time for a clear atmosphere (a) and for one with unit optical depth (b). Selected winds inferred from the entry data (dashed) are shown for comparison. For clarity, only one wind vector from the model calculations for optical depth 1 is shown because all winds in this region have similar directions and magnitudes.

heat fluxes produce a temperature profile at entry time that is only several degrees warmer than the smooth case.

Surface winds for the smooth, nominal, and rough cases are shown in Fig. 18. Smoother surfaces have stronger mean winds, larger diurnal variations, and earlier maxima. Since the column mean production of kinetic energy by pressure gradient force is unchanged by surface roughness, mean winds must increase over smooth terrain in order for surface drag to balance that production. Furthermore, since the forcing is the same, the diurnal variation must be larger.

The sense of rotation of the surface wind vector is relatively unchanged by surface roughness. For all roughness, the wind rotates counterclockwise with about the same phase. Only the size of the ellipse changes; smoother surfaces have larger ellipses. This dependence is similar to some of the cases explored by Hess et al. (1977), who used a simple model of an oscillating Ekman layer to describe the ellipse. Solutions of their model were sensitive to a "coupling factor" defined as the ratio of coupling strength to slope-induced pressure gradient. For small values of the coupling factor, the size of the ellipse increased with decreased damping. Since the damping in their model can be interpreted as surface drag, this result is consistent with ours and suggests that coupling is less important for the size of the ellipse than the slope-induced pressure gradient force.

### c. Visible-to-infrared optical depth

The spectral distribution of Martian dust opacity is not adequately known. Measurements of visible and infrared opacities during the Viking mission (Pollack et al. 1979; Martin 1986), and the apparent absence of a dust greenhouse effect (Haberle and Jakosky 1991), suggest that the ratio of visible-to-infrared opacity is near 2. This is the value we use in our nominal simulation. However, different particle size distributions can produce different ratios, and we have therefore explored the sensitivity of our results to values twice as large, and half as large, as the nominal value.

Increasing the ratio of visible-to-infrared opacity (Fig. 19) has a similar effect on the rotation of the surface wind vector, as does increasing the dust loading (Fig. 17). Daytime temperatures become warmer since the thermal emissivity of the atmosphere is diminished. This stabilizes the boundary layer and reduces its max-

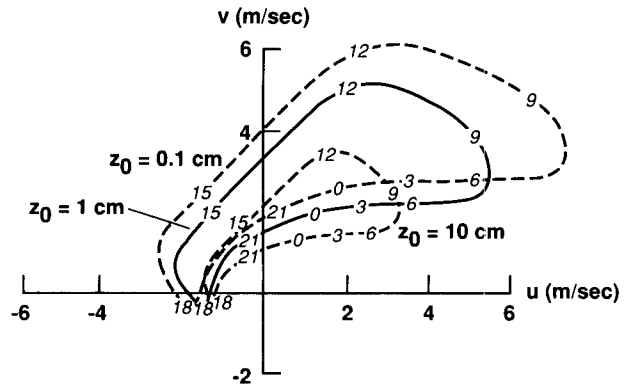


FIG. 18. As in Fig. 17 but for three different values of the surface roughness parameter 0.1, 1, and 10 cm.

imum depth. The weaker coupling to winds aloft allows the surface wind to develop more of an upslope-down-slope character.

## 5. Discussion

### a. Low-level nocturnal jets

A robust feature of all simulations is the development of low-level nocturnal jets. For the *VL-1* simulation, a closed jet of  $17 \text{ m s}^{-1}$  develops at the 100-m level just before dawn (Fig. 8b). At the same time, winds near the surface are relatively light (Fig. 6). Low-level nocturnal jets are commonly observed on Earth (e.g., Bonner 1968) and, for reasons to be discussed, they may be common on Mars as well.

Although several explanations for low-level jets have been suggested, the simplest—and most recognized—is that due to Blackadar (1957), who showed that boundary layers controlled by pressure gradient, Coriolis, and frictional forces can produce low-level jets if there is a significant diurnal variation of the eddy viscosity. A jet begins to develop when stabilization of

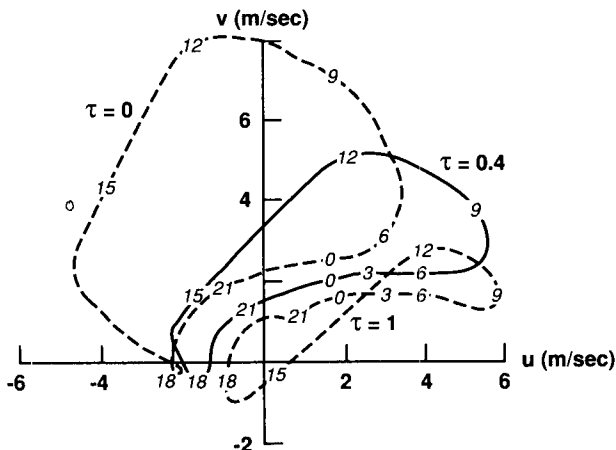


FIG. 17. Simulated *VL-1* 1.6-m hodographs for three different values of dust optical depth 0, 0.4, and 1.0. The solid line represents the nominal model.

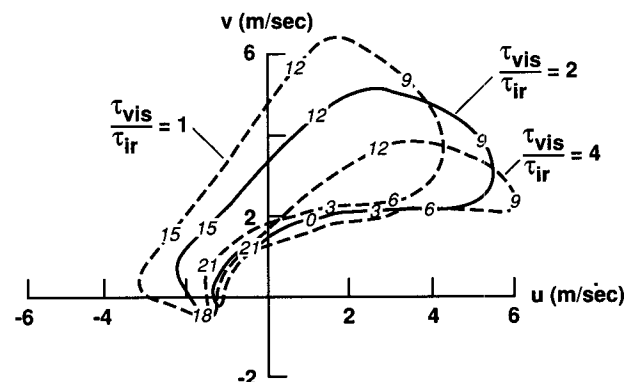


FIG. 19. As in Fig. 17 but for three different values of the ratio of visible to infrared optical depth 0.5, 1, and 4.

the boundary layer after sunset leaves the Coriolis and pressure gradient forces unbalanced. The winds are subsequently accelerated toward the existing geostrophic value by the resulting inertial oscillation. During the oscillation, the wind can exceed the geostrophic value. After sunrise, convection within the developing boundary layer destroys the jet and establishes a new imbalance.

Subsequent studies of Blackadar's mechanism by Thorpe and Guymet (1977) have shown that that jet development is favored when the initial force imbalance (i.e., the ageostrophic component) is large, the collapse of the boundary layer in the afternoon is rapid, and nights are long enough for the inertial oscillation to have an effect. Each of these conditions occurs on Mars. Vigorous daytime convection can produce a large ageostrophic wind, and there are few clouds to retard the afternoon surface cooling that causes boundary-layer collapse. Of course, during very dusty periods, afternoon cooling can be significantly reduced (Ryan and Henry 1979). Only near the equator and at high latitudes during summer are nights too short for the inertial oscillation to accelerate the winds. Thus, it appears that conditions favorable for low-level nocturnal jet development are prevalent on Mars.

#### b. Role of radiation

An interesting aspect of our simulations is the relative importance of radiation in controlling the structure of the boundary layer. For several hours after sunrise, the shallow but growing boundary layer warms mostly by convection due to convergence of the upward sensible heat flux. After 0900 LLT, however, radiative heating (infrared heating in particular) becomes the dominant warming mechanism. Ultimately, it becomes so strong that convection acts to cool rather than warm the lower levels. This is illustrated in Fig. 20 for the

early afternoon boundary layer and suggests that destabilization of the lower Martian atmosphere is due to radiation—not convection—and that convection is a response to the boundary-layer structure at this time rather than a driver of it. The contribution of radiation to the total heating of Earth's daytime boundary layer is negligible by comparison (Andre et al. 1978).

Above 500 m, the boundary layer continues to warm by both radiation and convection, but the latter now dominates. Radiation contributes about one-third of the total warming in that region and is mostly due to the absorption of solar radiation by dust. Thus, warming of the daytime boundary layer on Mars occurs in two distinct ways: in the lower part (<500 m) warming occurs by radiation that is strong enough to overcome cooling by convection; in the upper part (>500 m) warming occurs by convection, though radiation still makes a significant contribution.

After sunset the boundary layer cools, and again radiation is the dominant mechanism (Fig. 21). The boundary layer is very shallow at this time, and only very near the surface does the divergence of the sensible heat flux play a greater role. As the night progresses, however, the stable boundary layer grows as the shear stress increases. Turbulent heat losses become increasingly important and eventually dominate. A low-level inversion subsequently forms that by midnight has become strong enough for radiation emanating from its top to warm the lower levels. This trend is most pronounced just before dawn. Thus, in the well-developed nighttime boundary layer, turbulence is the driver and radiation is the response—opposite the daytime situation.

It is worth noting that while radiation drives turbulence during the day, winds drive it at night. The acceleration of low-level winds by the downslope-directed pressure gradient force increases the wind shear and surface stress. The resulting increase in heat loss

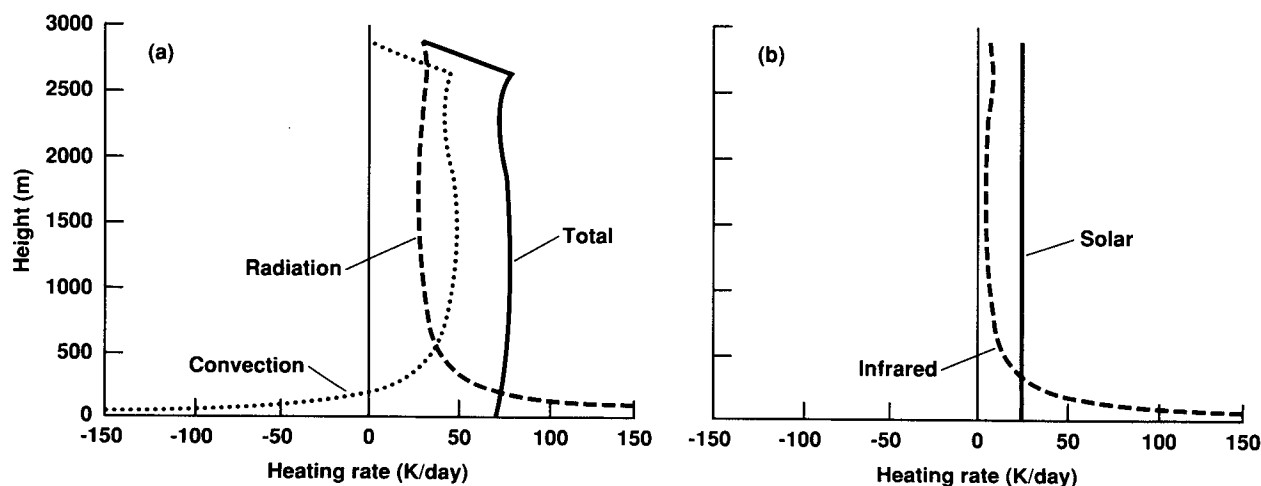


FIG. 20. Simulated daytime heating rates at V/L-1 in the lowest 3 km: (a) radiative (dashed), convective (dotted), and total (solid) heating rates and (b) the solar (solid) and infrared (dashed) contributions to the radiative heating rate.

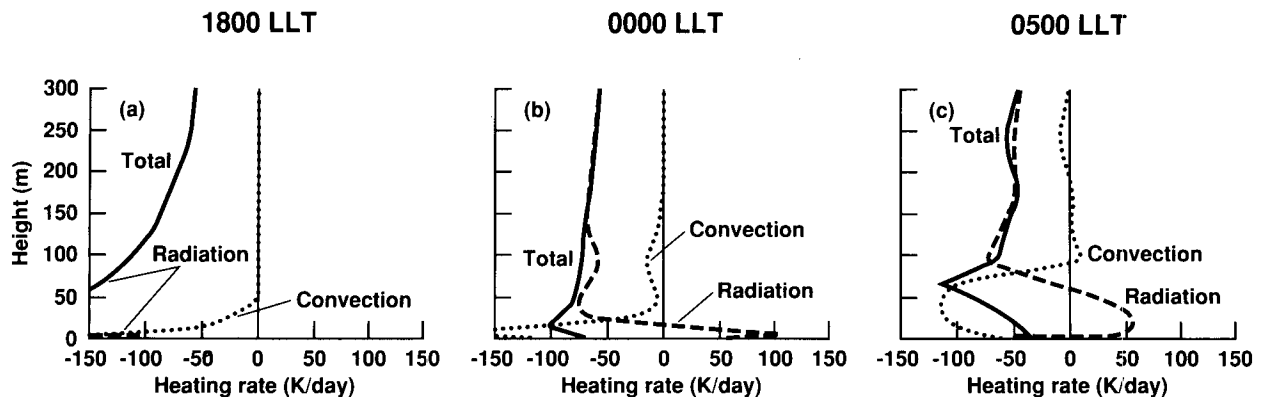


FIG. 21. As in Fig. 20a but for the lowest 300 m and for three different times of day: (a) early evening, 1800 LLT; (b) midnight, 0000 LLT; and (c) just before dawn, 0500 LLT.

and associated cooling further amplifies the downslope forcing. This feedback strengthens the inversion and helps produce the low-level radiative warming seen in Fig. 21.

#### c. Lander site slopes

The slopes we use for the lander sites differ from those reported by Hess et al. (1977). At *VL-1* we obtain best results when the slope magnitude is 0.003—a factor of 5 less than Hess et al. At *VL-2*, we require a different slope direction—downward toward the southwest rather than northwest. These are significant differences and reflect the limited physics contained in our model and/or the uncertainties in our knowledge of the lander site terrains.

The Hess et al. estimates were based on pre-Viking data. A newly derived Mars Digital Terrain Map (DTM) has been recently released that incorporates Viking radio occultations and stereo imaging pairs. This new dataset shows significant differences from the early data. However, the greatest uncertainties in the DTM data are at the intermediate horizontal scales (H. Kieffer, personal communication), and these are the scales that are relevant to our work (hundreds of kilometers).

There is also the possibility that topographic surfaces are not truly equipotential surfaces on Mars because of incomplete compensation. Balmino et al. (1982) present a spherical harmonic model of the Mars gravity field up to degree and order 18. An inspection of their Fig. 2 shows very little structure in the Martian geoid at the *VL-1* site. The largest slope in the geoid appears to be on the order of 0.0002, much less than the reported topographic slope. Thus, the issue of regional slopes for the lander sites will not be resolved until the *Mars Observer* spacecraft maps the surface in 1993–94.

#### d. Dust feedback effects

The major issue regarding the life cycle of global dust storms on Mars concerns the mechanisms for on-

set and decay [see Zurek et al. (1992) for a review of global dust storm theories]. Available data suggest that these storms loft huge quantities of dust into the atmosphere in a matter of days. Then, just as quickly, they cease lifting dust, and the atmospheric opacity begins a long exponential decline to prestorm values (Pollack et al. 1977; Murphy et al. 1990b).

Dust lofting is believed to occur by saltation, a process in which Martian fines are injected into the atmosphere when sand-sized particles some 100  $\mu\text{m}$  in diameter impart their kinetic energy to the smaller, more difficult-to-move fines after being momentarily suspended and then reimpacting the surface (Greeley and Iversen 1985). The movement of sand size particles begins when the friction velocity, or equivalently, the surface stress, reaches a threshold value, which for Mars lies between 1.5 and 2.5  $\text{m s}^{-1}$  (Iversen et al. 1976). Given the observed behavior of global dust storms, it appears that the friction velocity exceeds the threshold value in the source region for a relatively short period of time. The question is, Why does it increase and decrease so rapidly?

The increase in surface stress is believed to be a consequence of a general intensification of Martian wind systems (Leovy et al. 1973; Gierasch and Goody 1973). The intensification is partly due to the approach of the planet to perihelion, but more importantly, due to a positive feedback between dust and wind systems: the more dust in the atmosphere, the stronger the wind systems become, the more dust is lifted into the atmosphere, and so on. The intensification of large-scale wind systems with dust loading occurs in various models and supports the notion that positive feedbacks are an important part of the onset process (Haberle et al. 1982; Pollack et al. 1990; Murphy 1991). On the other hand, the decrease in stress is less well understood but is believed to be aided by the increase in static stability that accompanies an increasing dust load (e.g., Leovy et al. 1973). As the atmosphere stabilizes, turbulent mixing is suppressed, and the surface eventually decouples from the winds aloft.

Our model shows that surface winds (stresses) decrease in the presence of dust (see Fig. 17). To our knowledge, this is the first quantitative demonstration of this effect. However, there is an important caveat. Forcing of boundary-layer winds has been reduced in the dusty simulation, because the winds the surface couples to during the day are weaker. It is not clear, however, if this is due to stabilization or weaker forcing. To isolate the effect of stabilization, we have conducted simulations with constant forcing by eliminating the slope-induced pressure gradients and prescribing a time-independent pressure gradient equivalent to a geostrophic wind speed of  $5 \text{ m s}^{-1}$ . The results, which are shown in Fig. 22, confirm the role of stabilization in lowering the surface stress. Thus, this mechanism will contribute to the shut-off process.

What is not clear, however, is how the dust-raising wind system(s) will respond to the presence of dust. In the present case, we have shown that slope winds—at least to the extent we have modeled them—will be reduced in the presence of dust; other wind systems, however, may not. For example, the intensity of the zonal-mean meridional circulation computed by Haberle et al. (1982) shows no sign of decreasing with dust load; even for a global equivalent optical depth of 20, which is much greater than observed, the circulation is still strong. Similar results have been found in more recent calculations with the Mars General Circulation Model of Pollack et al. (1990). Thus, any shut-off mechanism must consider the effect of dust on the wind system as well as the temperature structure, since surface stresses ultimately depend on both.

## 6. Summary and conclusions

A boundary-layer model for Mars has been developed and compared with available observations. The model solves a momentum and heat equation and is designed to accept tracers as well. The momentum equation is standard for boundary-layer models and includes pressure gradient, Coriolis, and frictional

terms. However, the pressure-gradient force can be calculated as well as specified. To calculate it, we have developed a slope model similar to Blumsack et al. (1973), but in which the isotherms are assumed to exponentially approach a true horizontal (equipotential) surface with an adjustable  $e$ -folding depth. In our view, this leads to more realistic upper-level winds and is more consistent with the scales of motion that we are trying to simulate (hundreds of kilometers).

The model heat equation is also standard for boundary-layer models. It includes terms for turbulent, radiative, and advective heating. The latter only arises in the presence of sloping terrain and represents the adiabatic heating or cooling associated with downslope or upslope flow, respectively. Turbulent heating is due to the convergence of vertical fluxes, which like those for momentum, are calculated from the level-2 closure theory of Mellor and Yamada (1974). Though more sophisticated turbulence schemes are available, the Mellor and Yamada model contains the basic physics of shear and/or buoyancy-driven turbulence, and is simple to implement. Finally, the radiation term in the heat equation accounts for the absorption of solar and infrared radiation by dust and  $\text{CO}_2$  gas, the principal radiatively active constituents of the Martian atmosphere.

The main purpose of this paper has been to establish the model's regime of validity by comparing its predictions with available observations. The available data consist of two profiles of wind and temperature, and the near-surface diurnal variation of those parameters at two locations. The profiles were obtained during the parachute phase of the Viking landers descent to the surface and provide information between 1.5 and 4 km at each site. They were taken during afternoon at *VL-1* and morning at *VL-2*. The diurnal variations of near-surface parameters were obtained by the meteorology experiment, which measured wind and temperature at the 1.6-m level.

In general, the model reproduces the basic features of the temperature data. The agreement is particularly good at entry time for the *VL-2* site, where the model and observations are within several degrees at all levels for which data are available. This lends support to the model's prediction of an eroding low-level inversion at this time, but which is not evident in the entry data when temperatures are linearly interpolated to the surface. Such an interpolation is more justifiable at *VL-1* where deep convective mixing is likely at the time of entry. Convective mixing tends to produce temperature profiles that are close to adiabatic, and both model and observations show this to be the case although the model profiles tend to be less stable than observed. This is related to the tendency of the model to overestimate the near-surface diurnal amplitude.

At both sites, the model-simulated 1.6-m temperatures are higher than observed during the day and lower than observed at night. Since we have constrained the

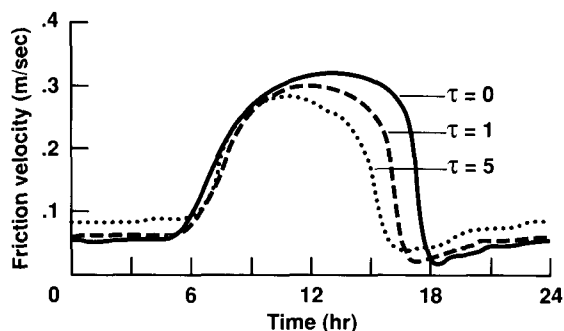


FIG. 22. Simulated diurnal variation of the friction velocity at *VL-1* for three different values of dust optical depth: 0 (solid), 1 (dashed), 5 (dotted). In these simulations the pressure gradient force is specified rather than calculated from the slope model. The pressure gradient is equivalent to a geostrophic wind of  $5 \text{ m s}^{-1}$ .

model to reproduce the observed ground temperatures, this deficiency must be due to the calculation of inaccurate energy fluxes into and out of the lowest model layer. We have speculated that the upward turbulent heat flux out of the lowest layer during day may be underestimated. This is consistent with the tendency of the level-2 turbulence scheme to underestimate the depth of Earth's convective boundary layer (Mellor and Yamada 1982).

Although the model can simulate some aspects of the observed winds, it is not able to simulate them all. In particular, we have been unable to find conditions under which the model can simultaneously reproduce the surface and entry data. For those simulations in which the model reproduces the surface data—counterclockwise rotation at *VL-1*, clockwise at *VL-2*, and a diurnal variation having about the same phase and amplitude as observed—it is unable to reproduce the entry data. At both sites the simulated entry winds are too weak. In the model, daytime mixing of momentum is so efficient that large shears in the low-level winds are never permitted to develop. Conversely, for those simulations in which the model reproduces the entry winds— $20 \text{ m s}^{-1}$  southeasterlies at *VL-1*, and  $8 \text{ m s}^{-1}$  north-northwesterlies at *VL-2*—the model is unable to reproduce the surface data. Again, because mixing is so efficient in the model, surface winds are too strong. Thus, the model either mixes momentum too efficiently, is lacking some additional vertically dependent forcing, or the single wind profile used for comparison is not representative of mean conditions.

An additional concern is the need to use different values of the slope parameters than those published by Hess et al. (1977). In our simulations, much gentler slopes are required at *VL-1*, while a different slope direction is required at *VL-2*. For the *VL-1* site, the available gravity data does indicate a sloping geoid, but the slope is small and cannot account for much of the discrepancy. For the *VL-2* site, we can simultaneously match the phase of the surface wind rotation and observed entry direction only if we assume a slope direction  $90^\circ$  from that reported. Thus, until better topography data become available, we cannot distinguish between model uncertainties and topographic uncertainties.

**Acknowledgments.** This work was supported by NASA's Planetary Atmospheres Program and the MSATT Mars Data Analysis Program. We have benefited from discussions with Alison Bridger, two anonymous reviewers, and Conway Leovy.

#### REFERENCES

- Andre, J. C., G. DeMoore, P. Lacarrere, G. Therry, and R. du Vachat, 1978: Modeling the 24-hour evolution of the mean and turbulent structures of the planetary boundary layer. *J. Atmos. Sci.*, **35**, 1862–1883.
- Arya, S. P., 1988: *Introduction to Micrometeorology*. Academic Press, 303 pp.
- Balmino, G., B. Moynot, and N. Vales, 1982: Gravity field model of Mars in spherical harmonics up to degree and order eighteen. *J. Geophys. Res.*, **87**, 9735–9746.
- Blackadar, A. K., 1957: Boundary layer wind maxima and their significance for the growth of nocturnal inversions. *Bull. Amer. Meteor. Soc.*, **38**, 283–290.
- , 1962: The vertical distribution of wind and turbulent exchange in the neutral atmosphere. *J. Geophys. Res.*, **67**, 3095–3102.
- Blumsack, S. L., P. J. Gierasch, and W. R. Wessel, 1973: An analytical and numerical study of the Martian planetary boundary layer over slopes. *J. Atmos. Sci.*, **30**, 66–82.
- Bonner, W. D., 1968: Climatology of the low-level jet. *Mon. Wea. Rev.*, **96**, 735–744.
- Crisp, D., 1986: Approximate methods for finding  $\text{CO}_2$  15- $\mu\text{m}$  band transmission in planetary atmospheres. *J. Geophys. Res.*, **91**, 11 851–11 866.
- Colburn, D. S., J. B. Pollack, and R. M. Haberle, 1989: Diurnal variations in optical depth at Mars. *Icarus*, **79**, 159–189.
- Flasar, F. M., and R. M. Goody, 1976: Diurnal behavior of water on Mars. *Planet. Space Sci.*, **24**, 161–181.
- Gierasch, P. J., and R. M. Goody, 1968: A study of the thermal and dynamical structure of the lower Martian atmosphere. *Planet. Space Sci.*, **16**, 615–646.
- , and R. M. Goody, 1972: The effect of dust on the temperature structure of the Martian atmosphere. *J. Atmos. Sci.*, **29**, 400–402.
- , and R. M. Goody, 1973: A model of a Martian great dust storm. *J. Atmos. Sci.*, **30**, 169–179.
- Goody, R. M., and M. J. S. Belton, 1967: Radiative relaxation times for Mars. *Planet. Space Sci.*, **15**, 247–256.
- Greeley, R., and J. D. Iversen, 1985: *Wind as a Geological Process*. Cambridge University Press, 333 pp.
- Haberle, R. M., and B. M. Jakosky, 1991: Atmospheric effects on the remote determination of thermal inertia of Mars. *Icarus*, **90**, 187–204.
- , C. B. Leovy, and J. B. Pollack, 1982: Some effects of global dust storms on the atmospheric circulation of Mars. *Icarus*, **50**, 322–367.
- Hess, S. L., R. M. Henry, C. B. Leovy, J. A. Ryan, and J. E. Tillman, 1977: Meteorological results from the surface of Mars: Viking 1 and 2. *J. Geophys. Res.*, **82**, 4559–4574.
- Holton, J. R., 1967: The diurnal boundary layer wind oscillation above sloping terrain. *Tellus*, **19**, 199–205.
- Iversen, J. D., R. Greeley, and J. B. Pollack, 1976: Windblown dust on Earth, Mars, and Venus. *J. Atmos. Sci.*, **33**, 2425–2429.
- Kieffer, H. H., T. Z. Martin, A. R. Peterfreund, B. M. Jakosky, E. D. Miner, and F. D. Palluconi, 1977: Thermal and albedo mapping of Mars during the Viking primary mission. *J. Geophys. Res.*, **82**, 4249–4291.
- Leovy, C. B., R. W. Zurek, and J. B. Pollack, 1973: Mechanisms for Mars dust storms. *J. Atmos. Sci.*, **30**, 749–762.
- Lettau, H. J., 1969: Note on aerodynamic roughness parameter estimation of roughness element description. *J. Appl. Meteor.*, **8**, 828–832.
- McNider, R. T., and R. A. Pielke, 1981: Diurnal boundary-layer development over sloping terrain. *J. Atmos. Sci.*, **38**, 2198–2212.
- Magalhaes, J., and P. Gierasch, 1982: A model of Martian slope winds: Implications for eolian transport. *J. Geophys. Res.*, **87**, 9975–9984.
- Mahrer, Y., and R. A. Pielke, 1977: The effects of topography on the sea and land breezes in a two-dimensional numerical mesoscale model. *Mon. Wea. Rev.*, **105**, 1151–1162.
- Martin, T. Z., 1986: Thermal infrared opacity of the Mars atmosphere. *Icarus*, **66**, 2–21.
- Mellor, G. L., and T. Yamada, 1974: A hierarchy of turbulence closure models for planetary boundary layers. *J. Atmos. Sci.*, **31**, 1791–1806.
- , and —, 1982: Development of a turbulence closure model for geophysical fluid problems. *Rev. Geophys. Space Phys.*, **20**, 851–875.
- Monin, A. S., and A. M. Yaglom, 1971: *Statistical Fluid Mechanics*. MIT Press, 417–526.
- Murphy, J. R., 1991: A dimensional hierarchy of numerical simu-

- lations of Martian global dust storms. Ph.D. thesis, University Washington, Seattle, 298 pp.
- , C. B. Leovy, and J. E. Tillman, 1990a: Observations of Martian surface winds at the Viking Lander 1 site. *J. Geophys. Res.*, **95**, 14 455–14 576.
- , O. B. Toon, J. B. Pollack, and R. M. Haberle, 1990b: Numerical simulations of the decay of Martian global dust storms. *J. Geophys. Res.*, **95**, 14 629–14 648.
- Pallman, A. J., 1983: The thermal structure of the atmospheric surface layer on Mars as modified by the radiative effect of Aeolian dust. *J. Geophys. Res.*, **88**, 5483–5493.
- Pollack, J. B., D. S. Colburn, R. Kahn, J. Hunter, W. Van Camp, C. E. Carlston, and M. R. Wolfe, 1977: Properties of aerosols in the Martian atmosphere as inferred from Viking lander imaging data. *J. Geophys. Res.*, **82**, 4479–4496.
- , —, F. M. Flasar, R. R. Kahn, C. E. Carlston, and D. Pidek, 1979: Properties and effects of dust particles suspended in the Martian atmosphere. *J. Geophys. Res.*, **84**, 2929–2945.
- , C. B. Leovy, P. W. Greiman, and Y. Mintz, 1981: A Martian general circulation experiment with large topography. *J. Atmos. Sci.*, **38**, 3–29.
- , R. M. Haberle, J. Schaeffer, and H. Lee, 1990: Simulations of the general circulation of the Martian atmosphere I: Polar Processes. *J. Geophys. Res.*, **95**, 1447–1474.
- Ryan, J. A., and R. M. Henry, 1979: Mars atmospheric phenomena during major dust storms, as measured at surface. *J. Geophys. Res.*, **84**, 2821–2829.
- Seiff, A., and D. B. Kirk, 1977: Structure of the atmosphere of Mars in Summer at mid-latitudes. *J. Geophys. Res.*, **82**, 4364–4378.
- , 1993: Mars atmospheric winds indicated by motion of the Viking landers during parachute descent. *J. Geophys. Res.*, in press.
- Sutton, J. L., C. B. Leovy, and J. E. Tillman, 1978: Diurnal variation of the martian surface layer meteorological parameters during the first 45 sols at two Viking lander sites. *J. Atmos. Sci.*, **35**, 2346–2355.
- Thorpe, A. H., and T. H. Guymer, 1977: The nocturnal jet. *Quart. J. Roy. Meteor. Soc.*, **103**, 633–653.
- Toon, O. B., J. B. Pollack, and C. Sagan, 1977: Physical properties of the particles comprising the Martian dust storm of 1971–1972. *Icarus*, **30**, 663–696.
- Ye, Z. J., M. Segal, and R. A. Pielke, 1990: A comparative study of daytime thermally induced upslope flow of Mars and Earth. *J. Atmos. Sci.*, **47**, 612–628.
- Zurek, R. W., J. R. Barnes, R. M. Haberle, J. B. Pollack, J. E. Tillman, and C. B. Leovy, 1992: Dynamics of the atmosphere of Mars. *Mars*, H. H. Kieffer, B. M. Jakoskv, C. W. Snyder, and M. S. Matthews, Eds., University of Arizona Press, 835–933.